SUPPLEMENTARY INFORMATION

Tailoring a fluorophosphate as a novel 4 V cathode for lithium-ion batteries

Young-Uk Park[1], Dong-Hwa Seo[1], Byoungkook Kim[2], Kun-Pyo Hong[3,4], Hyungsub Kim[1], Seongsu Lee[3], Rana A. Shakoor[5], Keiichi Miyasaka[5], Jean-Marie Tarascon[6] and Kisuk Kang[1,7,*]

[1]Department of Materials Science and Engineering, Seoul National University, Gwanak-ro 1, Gwanak-gu, Seoul 151-742, Korea

[2]Research Analysis Center, KAIST, Daehak-ro 291, Yuseong-gu, Daejeon 305-701, Korea

[3]Korea Atomic Energy Research Institute, P.O. Box 105, Yuseong-gu, Daejeon 305-600, Korea

[4]Graduate School of Green Energy Technology, Chungnam National University, Daehak-ro 99, Yuseong-gu, Daejeon 305-764, Korea

[5]Graduate School of EEWS (WCU), KAIST, Daehak-ro 291, Yuseong-gu, Daejeon 305-701, Korea

[6]Université de Picardie Jules Verne, CNRS UMR 7314, 33 rue Saint Leu, 80039 Amiens, France

[7]Research Institute of Advanced Materials, Seoul National University, Gwanak-ro 1, Gwanak-gu, Seoul 151-742, Korea

*e-mail: matlgen1@snu.ac.kr

Chapter 1) Search for the optimum fluorine substitution in Na$_{1.5}$VPO$_{5-\delta}$F$_{0.5+\delta}$

To adjust the stoichiometric ratio of fluorine and oxygen in the structure, we systematically changed the precursor ratio in the synthesis. In other words, we increased δ (from zero to unity) in the reaction of "$(1 - \delta)$V^{5+}PO$_5$ + δV^{3+}PO$_4$ + $(0.5+\delta)$NaF + $[(1 - \delta)/2]$Na$_2$CO$_3$" to obtain a series of fluorinated Na$_{1.5}$VPO$_{5-\delta}$F$_{0.5+\delta}$ having different degrees of fluorine substitution (denoted as δ). Use of (V^{4+}O)$_2$P$_2$O$_7$ instead of V^{5+}PO$_5$ always yielded the same result (even when $\delta = 0$), but we used V^{5+}PO$_5$ because the synthesis of the (V^{4+}O)$_2$P$_2$O$_7$ requires cost-ineffective inert atmosphere. For this reason, the terminology "V^{4+} precursor" (used in the text) means V^{5+}PO$_5$ rather than (V^{4+}O)$_2$P$_2$O$_7$. The corresponding cell parameters of each sample were obtained by full pattern matching of the neutron diffraction (ND) patterns. Figure S1a shows that lattice parameters of a product with $\delta = 0.2$ are in between those of non-fluorinated Na$_{1.5}$VPO$_5$F$_{0.5}$ ($\delta = 0$) and fully fluorinated Na$_{1.5}$VPO$_4$F$_{1.5}$ ($\delta = 1$), reminiscent of their solid-solution phase (without impurities, as shown in Figure 1b in the text).

We tried to obtain more fluorinated samples ($\delta > 0.2$ in Na$_{1.5}$VPO$_{5-\delta}$F$_{0.5+\delta}$) by attempting a reaction of "0.7V^{5+}PO$_5$ + 0.3V^{3+}PO$_4$ + 0.8NaF + 0.35Na$_2$CO$_3$", but we failed to get a pure target phase (Figure S1b). Even though the main phase was the target phase (Na$_{1.5}$VPO$_{5-\delta}$F$_{0.5+\delta}$, no symbol), a considerable amount of impurity phases, such as Na$_3$V$_2$(PO$_4$)$_3$ (blue circles), V$_2$O$_3$ (green arrows), and VO$_2$ (orange asterisks), were detected. This means that, due to the solubility limit, we failed to obtain a pure solid-solution phase ($\delta = 0.3$) between Na$_{1.5}$V^{4+}PO$_5$F$_{0.5}$ and Na$_{1.5}$V^{3+}PO$_4$F$_{1.5}$ (target ratio = 7:3) using the stoichiometric combination of precursors. Therefore, we determined that $\delta = 0.2$ was the maximum fluorine content that would not generate second phases. Further substitution of fluorine resulted in a substantial fraction of impurity phases.

Finally, we experimentally determined the chemical compositions of three sodium phases having different degrees of fluorination ($\delta = 0$, 0.2, and 1) using inductively coupled plasma (ICP) spectroscopy and energy-dispersive X-ray spectroscopy (EDS) analyses. The contents (in wt%) of Na, V, and P were determined via ICP spectroscopy while those of anions (O and F) were carefully

estimated by calculating O/V and F/V ratios from the EDS quantification results (see Figure S1c). From the two complementary quantification tools, we found that the average chemical compositions of the sodium phases were not considerably different from their theoretical compositions; $Na_{1.47(\pm 0.02)}V_{1.00}P_{1.00(\pm 0.01)}O_{4.96(\pm 0.07)}F_{0.52(\pm 0.05)}$ for $\delta = 0$, $Na_{1.48(\pm 0.02)}V_{1.00}P_{1.00(\pm 0.01)}O_{4.78(\pm 0.06)}F_{0.74(\pm 0.04)}$ for $\delta = 0.2$, and $Na_{1.52(\pm 0.03)}V_{1.00}P_{1.00(\pm 0.01)}O_{3.95(\pm 0.08)}F_{1.54(\pm 0.07)}$ for $\delta = 1$.
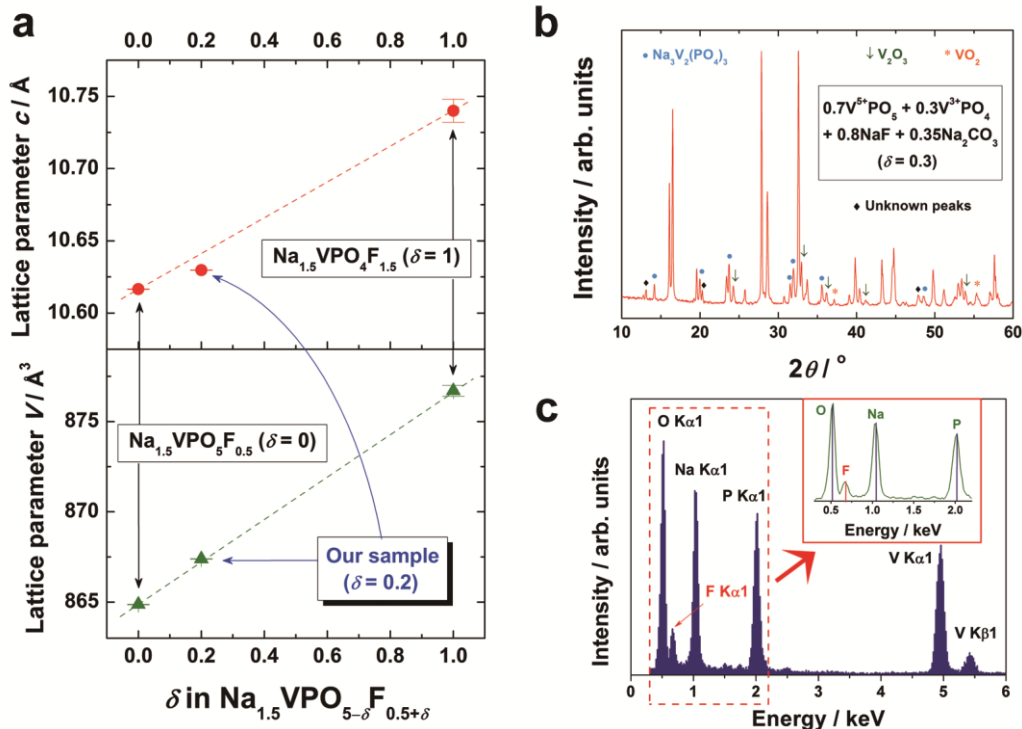

Figure S1. (a) Variation in the lattice parameter c and V of $Na_{1.5}VPO_5F_{0.5}$ ($\delta = 0$), $Na_{1.5}VPO_4F_{1.5}$ ($\delta = 1$), and our sample ($\delta = 0.2$) determined from the ND data (see Chapter 2). The cell parameters for each sample were calculated by performing the refinement (full pattern matching) with the space group $P4_2/mnm$. Red circles and green triangles denote lattice parameters c and V, respectively. (b) XRD pattern of the product after heat treatment (750℃, 1.5 hours, Ar) of the precursor combination of "$0.7V^{5+}PO_5 + 0.3V^{3+}PO_4 + 0.8NaF + 0.35Na_2CO_3$ ($\delta = 0.3$)". (c) An EDS spectrum of the single-crystalline $Na_{1.5}VPO_{4.8}F_{0.7}$ particle in the inset of Figure 1b in the text. The overall spectrum (0–6 keV) and an enlarged spectrum (0.3–2.2 keV, inset) show that the EDS peaks of all elements in our samples (Na, V, P, O, and F) are well separated. We believe that this makes the O and F quantification results from EDS spectra more reliable.

Chapter 2) Structural determination of $Na_{1.5}VPO_{4.8}F_{0.7}$

The structural refinement of $Na_{1.5}VPO_{4.8}F_{0.7}$ was carried out by the Rietveld method using Fullprof software[1]. The refinement results are shown in Tables S1 and S2. A structure model was constructed from the ND Rietveld refinement. In particular, the atomic position and the atomic displacement parameter of vanadium were complementarily determined from the XRD Rietveld refinement because its nuclei scarcely scatter neutrons[2] (see Figure S2 for the XRD pattern of $Na_{1.5}VPO_{4.8}F_{0.7}$ and its Rietveld refinement). Both the O4 and F2 sites (two terminal positions of the $V_2O_{10}F$ bioctahedron, as shown in Figure 1a in the text) were crystallographically identical having occupancies of 0.8 and 0.2 (based on elemental analysis), respectively. Na^+ ions were located at two different crystallographic sites in the *ab* plane (Figure S3), referred to as Na1 and Na2, with occupancies of 0.88 and 0.62, respectively. Both sites have a similar local environment, surrounded by seven oxygen and fluorine anions forming an augmented triangular prism. However, Na^+ ions in the Na1 site lie near the center of the prism, while those in the Na2 site are away from the center.

X-ray photoelectron spectroscopy (XPS) is an effective tool to investigate the local state of element. One can compare either the local bonding or the oxidation state of a specific element in samples with relatively good accuracy[3-5]. The phosphorus $2p$ binding energies of $Na_{1.5}VPO_5F_{0.5}$ and $Na_{1.5}VPO_{4.8}F_{0.7}$ were same (132.6 eV) in the XPS spectra (Figure S4), which suggests that both have identical PO_4 tetrahedral environments[6]. While all other oxygen ions in the $V_2O_{10}F$ bioctahedra share corners of PO_4 tetrahedra, the two terminal oxygens (denoted by arrows in Figure 1a in the text) are relatively unbound in the crystal. The invariance of phosphorus $2p$ binding energies for the PO_4 tetrahedra implies that the substitution of fluorine for one of the oxygens in PO_4 is quite unlikely.

Table S1. Lattice parameters and cell volumes for $Na_{1.5}VPO_{4.8}F_{0.7}$

Space Group	$P4_2/mnm$
Cell parameters	
a (Å)	9.0332(1)
b (Å)	9.0332(1)
c (Å)	10.6297(2)
α (°)	90(-)
β (°)	90(-)
γ (°)	90(-)
Volume (Å^3)	867.37(2)
Reliability factors	
R_P (%)	2.83
R_I (%)	3.20
R_F (%)	2.79

Table S2. Atomic positions for $Na_{1.5}VPO_{4.8}F_{0.7}$

Label	*Atom*	*Site*	*x*	*y*	*z*	*Occupancy*	B_{iso} (Å^2)
Na1	Na	*8i*	0.5110(4)	0.239(1)	0 (-)	0.88(1)	0.92(9)
Na2	Na	*8i*	0.8075(8)	0.0344(8)	0 (-)	0.62(1)	1.7(2)
V1	V	*8j*	0.2477(3)	0.2477(3)	0.19628(8)	1	0.74(3)
P1	P	*4d*	0 (-)	½ (-)	¼ (-)	1	0.16(3)
P2	P	*4e*	0 (-)	0 (-)	0.2561(5)	1	0.16(3)
O1	O	*16k*	0.0979(4)	0.4055(3)	0.1641(4)	1	0.17(5)
O2	O	*8j*	0.0954(4)	0.0954(4)	0.1686(5)	1	0.85(6)
O3	O	*8j*	0.4050(4)	0.4050(4)	0.1564(5)	1	0.85(6)
O4	O	*8j*	0.2470(4)	0.2470(4)	0.3548(1)	0.8	1.00(3)
F1	F	*4f*	0.2488(5)	0.2488(5)	0 (-)	1	0.25(4)
F2	F	*8j*	0.2470(4)	0.2470(4)	0.3548(1)	0.2	1.00(3)

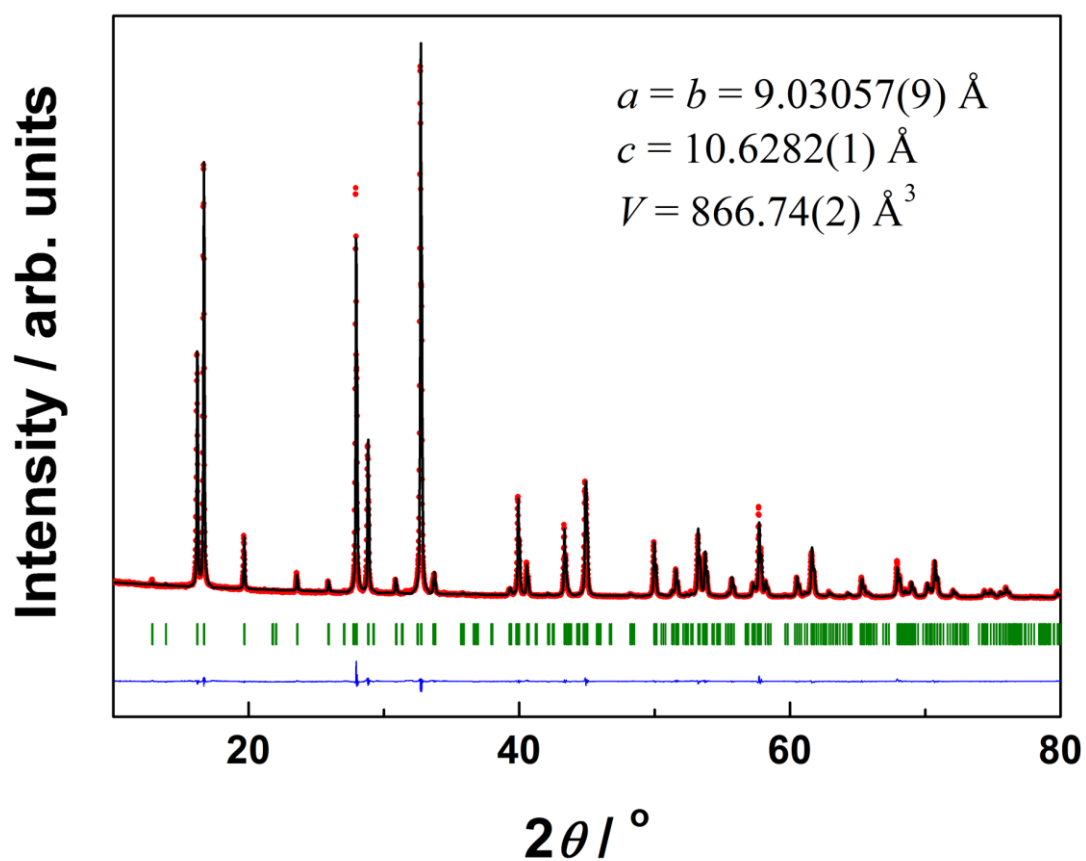**Figure S2.** XRD pattern of $Na_{1.5}VPO_{4.8}F_{0.7}$ and its Rietveld refinement in the $P4_2/mnm$ space group with observed data points (red dots), calculated pattern (black line), difference curve (blue line), and Bragg positions (green bars); lattice parameters are $a = b = 9.03057(9)$ Å, $c = 10.6282(1)$ Å, and $V = 866.74(2)$ Å^3.
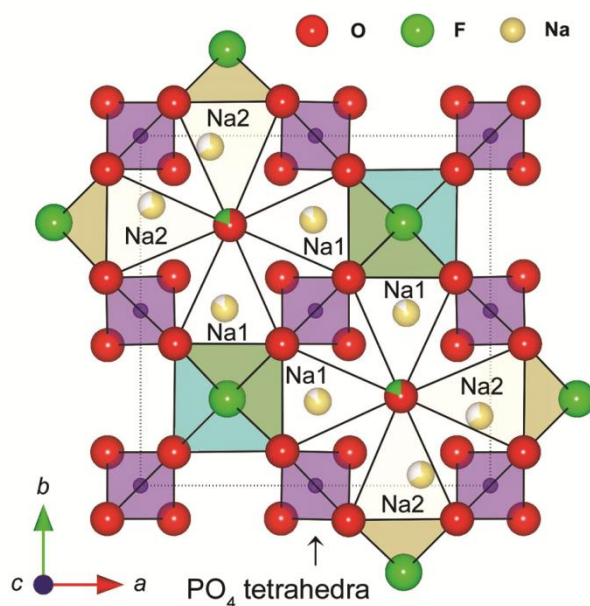
Figure S3. Illustration of the configuration of Na^+ ions in the *ab* plane. The white regions in the Na sites denote the vacancy fraction.
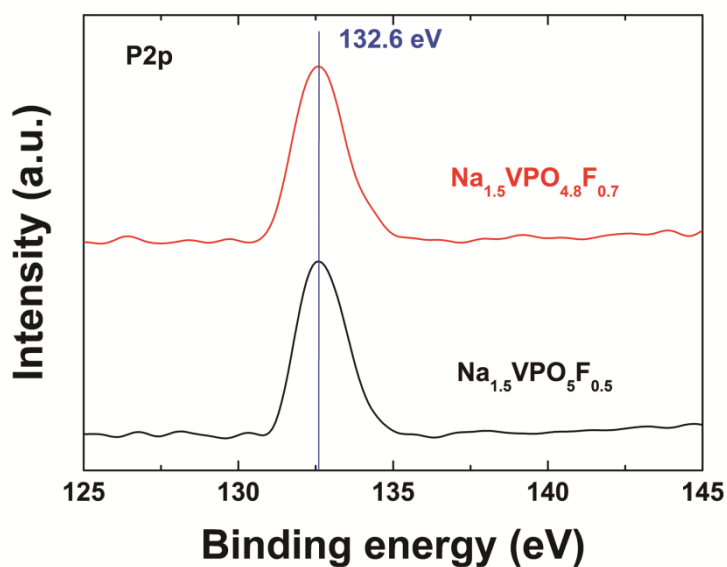

Figure S4. Comparison of P2*p* binding energies in XPS spectra of the pristine sodium phase ($Na_{1.5}VPO_5F_{0.5}$, bottom) and the fluorine substituted phase ($Na_{1.5}VPO_{4.8}F_{0.7}$, top). The identical XPS P2*p* binding energy implies that all phosphorus ions have the same local environment surrounded by four oxygen ions, i.e., PO_4 tetrahedra.

Chapter 3) Quantification of the average oxidation state of vanadium by the double titration method

We used the double titration method[7] to quantify the average oxidation state of vanadium ions in samples with high accuracy. We summarized the detailed experimental procedure in Figure S5.

Table S3 shows the average oxidation state of vanadium (AV) for various vanadium-containing compounds determined by the double titration method. The AV values of $Na_{1.5}VPO_5F_{0.5}$ and $Na_{1.5}VPO_4F_{1.5}$ were +4.07 and +2.99, respectively, and were very similar to the theoretical values (+4 and +3). The AV value of our sample ($Na_{1.5}VPO_{4.8}F_{0.7}$) was ca. +3.8, suggesting that V^{3+} and V^{4+} ions are mixed in the crystal at a ratio of 1:4. Also, it is in good agreement with the oxygen and fluorine quantification results in Chapter 1. Additionally, AV values for other well-known vanadium-containing compounds (Table S3) were almost identical to their theoretical values, confirming the reliability of this method.

Table S3. Average oxidation state of vanadium (AV) for various vanadium-containing compounds determined by the double titration method

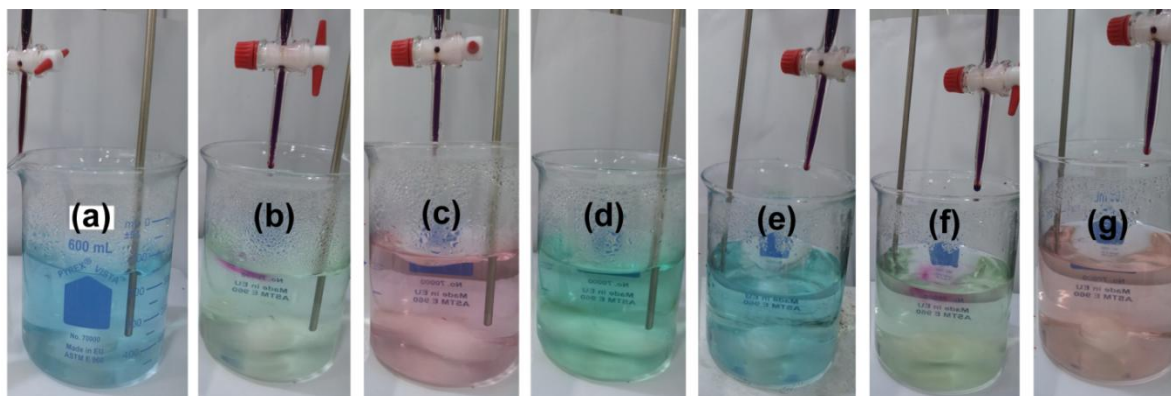| Sample	AV	Synthetic route
$Na_{1.5}VPO_4F_{1.5}$	+2.99	$V^{3+}PO_4$ + 1.5NaF (750℃, 1.5 h, Ar)
$Na_{1.5}VPO_5F_{0.5}$	+4.07	$V^{5+}PO_5$ + 0.5NaF + 0.5Na_2CO_3 (750℃, 1.5 h, Ar)
$Na_{1.5}VPO_{4.8}F_{0.7}$ (our sample)	**+3.76**	0.8$V^{5+}PO_5$ + 0.2$V^{3+}PO_4$ + 0.7NaF + 0.4Na_2CO_3 (750℃, 1.5 h, Ar)
$Li_3V_2(PO_4)_3$	+2.98	Reference 8
V_2O_3	+2.97	Aldrich

Figure S5. Photographs representing the experimental procedure of the double titration method. (a) Vanadium-containing compounds are completely dissociated or ionized in 2 M H_2SO_4 solution at 80°C. Colors of V^{3+}, V^{4+}, and V^{5+} ions in aqueous solution are generally known to be green, blue, and yellow, respectively. (b) The first titration with the 0.1 N $KMnO_4$ solution was not stopped until the overall color of the solution abruptly changed to purple (corresponding to complete oxidation of V^{x+} to V^{5+}). (c) The first titration was halted, and the total volume of the $KMnO_4$ solution consumed during the first titration (V_1) was measured. (d) An excess amount of $FeSO_4(NH_4)_2(SO_4)\cdot6H_2O$ was added to the solution to reduce all V^{5+} ions to V^{4+} ions by the Fe^{2+}/Fe^{3+} redox couple. (e) After the entire solution was cooled to room temperature, an excess amount of $(NH_4)_2S_2O_8$ was added to fully oxidize residual Fe^{2+} ions to Fe^{3+} ions for the accuracy of the second titration. (f) The second titration with the 0.1 N $KMnO_4$ solution was not stopped until the overall color of the solution abruptly changed to purple (corresponding to complete oxidation of V^{4+} to V^{5+}). (g) The second titration was halted, and the total volume of the $KMnO_4$ solution consumed during the second titration (V_2) was measured. Finally, the average oxidation state of vanadium (AV) was calculated by the equation "AV = $5 - V_1/V_2$".

Chapter 4) Experimental conditions for ion-exchange

Several ion-exchange conditions were explored to optimize the degree of the process; detailed data are shown in Table S4. Elemental quantification (lithium, sodium, vanadium, and phosphorus) was carried out using ICP spectroscopy. All other products, except for the one prepared via the molten salt method, retained the initial structure, as confirmed by XRD measurements (not shown here).

Table S4. Comparison of the degree of Na^+/Li^+ ion-exchange (i.e., the exchanged amount) for a variety of experimental conditions

Ionic conducting solvent	*Reaction temp. ($^{\bullet}C$)*	*Reaction time (h)*	*Lithium source*	*Li*	*Na*	*V*	*P*
Ethanol	70	17	LiBr	0	1.5	1.0	1.0
Acetonitrile	85	17	LiBr	0.5	1.0	1.0	1.0
1-hexanol	160	6–17	LiBr	1.1	0.4	1.0	1.0
$LiCl/LiNO_3$ molten	280	5	$LiCl/LiNO_3$	Phase decomposition			

Our findings through these experiments are as follows:

i.   Ion-exchange conditions that are too mild (e.g., using ethanol or acetonitrile as the ionic conducting solvents) could substitute no more than 0.5 Li^+ ions for Na^+ ions.

ii.   Too harsh conditions (e.g., using $LiCl/LiNO_3$ molten salt) caused phase decomposition.

iii. Only the ion-exchange conditions using 1-hexanol with a reaction time of 6–17 hours yielded sufficient Na^+/Li^+ ion exchange (ca. 1.1).

iv.   Considering that the ion-exchanged phase ($Li_{1.1}Na_{0.4}VPO_{4.8}F_{0.7}$) is thermally stable up to 550℃ (see Figure 3d in the text), the phase decomposition at 280℃ suggested that a minimum amount of Na^+ ions in the metastable phase is necessary to maintain structural integrity.

Chapter 5) Structural determination of $Li_{1.1}Na_{0.4}VPO_{4.8}F_{0.7}$

The ND pattern of $Li_{1.1}Na_{0.4}VPO_{4.8}F_{0.7}$ was successfully refined with the same space group ($P4_2/mnm$) as $Na_{1.5}VPO_{4.8}F_{0.7}$ (Tables S5 and S6), with negligible change in the structure: an identical structure model (including the O4 and F2 sites) was used for both. Thus, major structural changes[9, 10] do not accompany the ion-exchange process. The atomic position and the atomic displacement parameter of vanadium were also determined from the XRD Rietveld refinement (see Figure S10a), while those of lithium were determined from the ND Rietveld refinement. This complementary XRD-ND co-refinement was especially effective in our case where the target phase contains both vanadium and lithium, because it is well known that neutron is less sensitive to vanadium whereas X-ray is not sensitive to lithium. Supposing that the number of the Na^+ ions exchanged for Li^+ ions was 1.1 (per the ICP spectroscopy results), we investigated which site the newly introduced Li^+ ions preferred by refining the occupancies of the Li1/Na1 and Li2/Na2 sites (corresponding to the Na1 and Na2 sites in $Na_{1.5}VPO_{4.8}F_{0.7}$, respectively). The Li^+ ions seemed to strongly prefer the former to the latter, while the Na^+ ions were seldom located in the former. Hence, the Li1/Na1 site was fully occupied solely by Li^+ ions whereas the Li2/Na2 site was partially filled with both Li^+ and Na^+ ions. Figure S6 shows the alkali metal layer in the *ab* plane with the local environments of the two kinds of sites. The configuration of the alkali ions resembles the parent sodium phase (see Figure S3), implying facile two-dimensional diffusion of mobile ions (refer to Figure 5a in the text). Using the theoretical molecular weight (188.84 g mol^{-1}) calculated for the composition $Li_{1.1}Na_{0.4}VPO_{4.8}F_{0.7}$, its unit cell volume (843.24 $Å^3$), and the number of motifs per unit cell ($Z = 8$), we calculated a relatively low theoretical density of 3.0 g cm^{-3} for the material. This result implies that it has a more spacious structure than other conventional cathode materials (cf., 3.6 g cm^{-3} for $LiFePO_4$ and 5.1 g cm^{-3} for $LiCoO_2$)[11].

Table S5. Lattice parameters and cell volumes for $Li_{1.1}Na_{0.4}VPO_{4.8}F_{0.7}$

Space Group	$P4_2/mnm$
Cell parameters	
a (Å)	8.9836(6)
b (Å)	8.9836(6)
c (Å)	10.4483(8)
α (°)	90(-)
β (°)	90(-)
γ (°)	90(-)
Volume (Å^3)	843.24(9)
Reliability factors	
R_P (%)	5.31
R_I (%)	8.17
R_F (%)	5.39

Table S6. Atomic positions for $Li_{1.1}Na_{0.4}VPO_{4.8}F_{0.7}$

Label	Atom	Site	x	y	z	Occupancy
Li1	Li	*8i*	0.462(2)	0.258(3)	0 (-)	0.968(9)
Na1	Na	*8i*	0.462(2)	0.258(3)	0 (-)	0.032(9)
Li2	Li	*8i*	0.722(7)	0.021(8)	0 (-)	0.134(9)
Na2	Na	*8i*	0.722(7)	0.021(8)	0 (-)	0.366(9)
V1	V	*8j*	0.248(2)	0.248(2)	0.2028(4)	1
P1	P	*4d*	0 (-)	½ (-)	¼ (-)	1
P2	P	*4e*	0 (-)	0 (-)	0.259(2)	1
O1	O	*16k*	0.097(2)	0.408(2)	0.159(2)	1
O2	O	*8j*	0.095(3)	0.095(3)	0.167(3)	1
O3	O	*8j*	0.397(3)	0.397(3)	0.142(4)	1
O4	O	*8j*	0.241(3)	0.241(3)	0.3508(9)	0.8
F1	F	*4f*	0.256(3)	0.256(3)	0 (-)	1
F2	F	*8j*	0.241(3)	0.241(3)	0.3508(9)	0.2
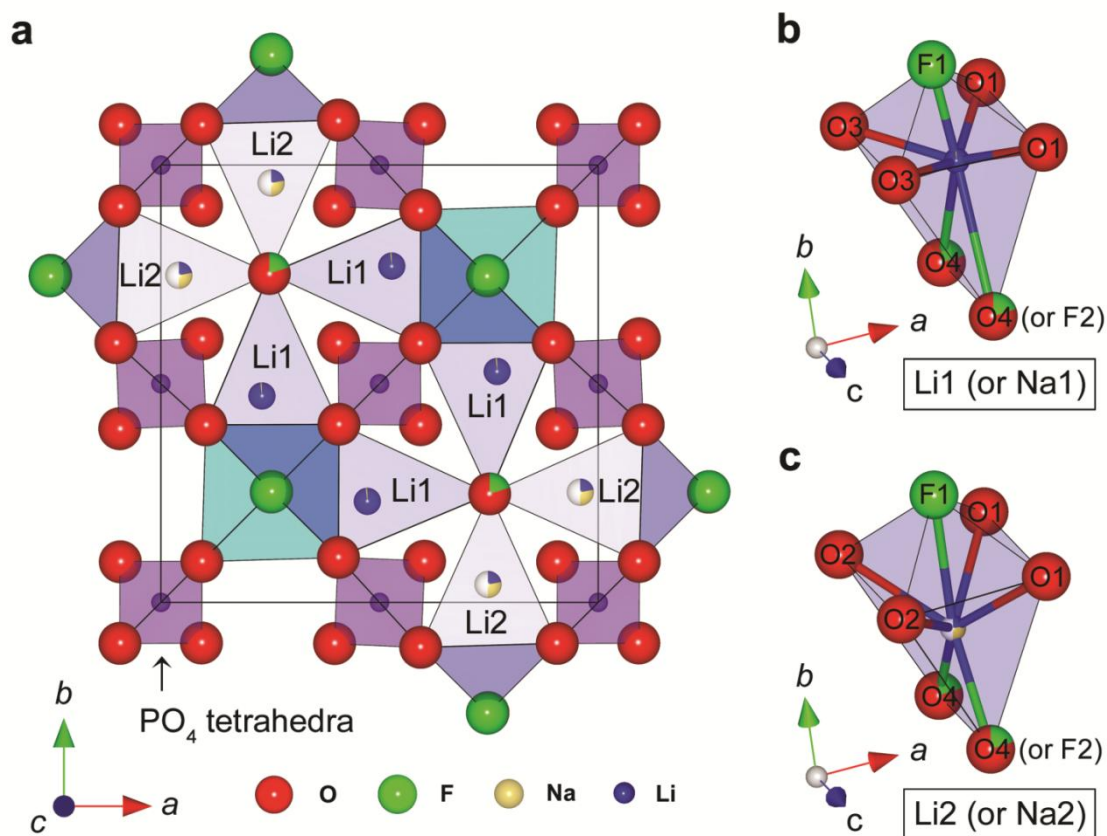
Figure S6. (a) Configuration of Li$^+$ and Na$^+$ ions in the *ab* plane in Li$_{1.1}$Na$_{0.4}$VPO$_{4.8}$F$_{0.7}$ and the corresponding local environments of (b) Li1 (or Na1) and (c) Li2 (or Na2) sites drawn based on the refinement results (Tables S5 and S6). Li, Na, P, O, and F atoms are shown in blue, yellow, purple, red, and green, respectively. Partially occupied sites (Li/Na) are denoted as multicolored spheres. The relative amounts of blue and yellow areas in each site indicate the extent of occupancy by Li$^+$ and Na$^+$ ions, respectively. White regions denote the vacancy fraction.

Chapter 6) Transmission electron microscopy (TEM) study of Li$_{1.1}$Na$_{0.4}$VPO$_{4.8}$F$_{0.7}$ particles

Bright-field TEM images (Figure S7a–c) show that the particle sizes of Li$_{1.1}$Na$_{0.4}$VPO$_{4.8}$F$_{0.7}$ were in the micron range. Their respective SAED patterns (Figure S7d–f) suggest that all of the microcrystallites were single crystals because only spot patterns rather than ring patterns were observed throughout a single particle. All of the spots in the SAED patterns could be indexed using the lattice parameters and (*hkl*) indices of Li$_{1.1}$Na$_{0.4}$VPO$_{4.8}$F$_{0.7}$ obtained from the refinement results of ND patterns (see Chapter 5), and each zone axis was determined by means of the Weiss zone law.
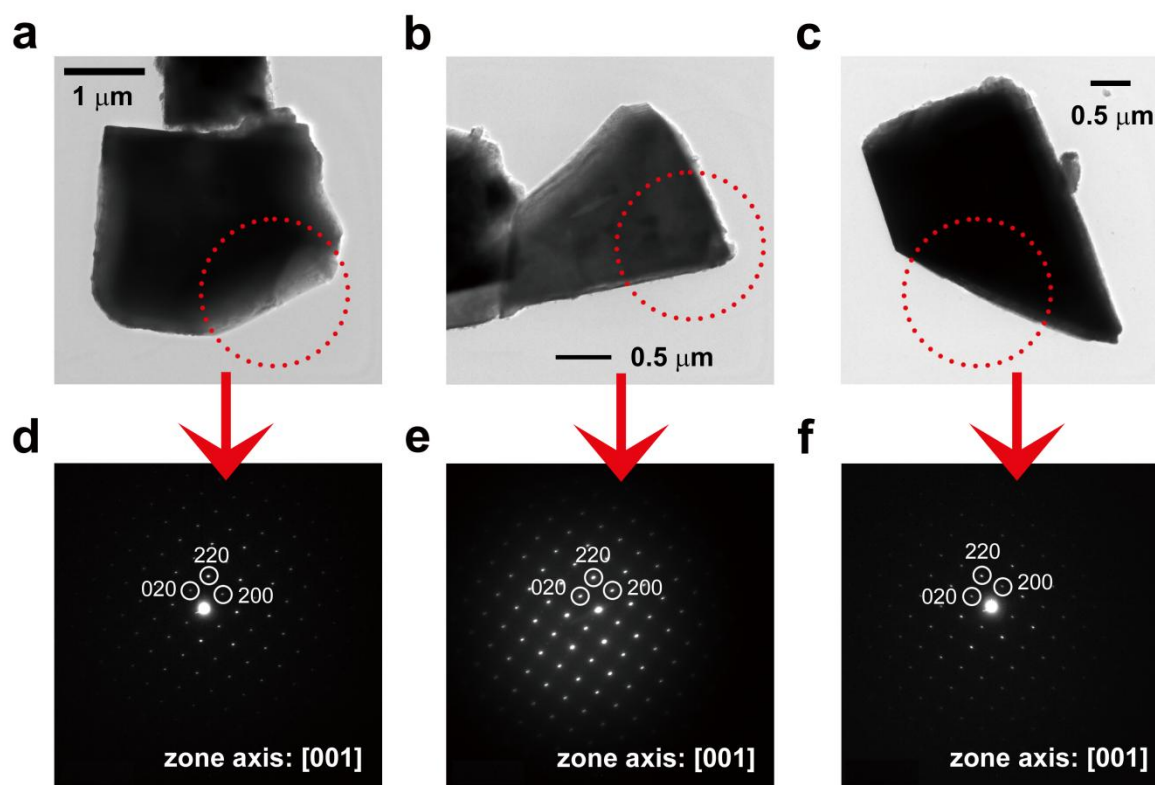
Figure S7. (a–c) Bright-field TEM images and (d–f) the corresponding SAED patterns of Li$_{1.1}$Na$_{0.4}$VPO$_{4.8}$F$_{0.7}$.

Chapter 7) ^{23}Na magic angle spinning (MAS) nuclear magnetic resonance (NMR) studies of $Na_{1.5}VPO_{4.8}F_{0.7}$ and $Li_{1.1}Na_{0.4}VPO_{4.8}F_{0.7}$

Most transition metal-containing positive electrode materials for lithium-ion batteries are paramagnetic, so isotropic shifts in their ^{6}Li MAS NMR spectra principally arise from Fermi contact interactions. This interaction causes a net electron spin around the lithium nuclei and hence leads to large hyperfine shifts[12, 13]. According to the Goodenough–Kanamori superexchange rules[14] and their modified theory[13], the amount of the net spins transferred from M t_{2g} or e_g orbitals (M = paramagnetic transition metals) to Li $2s$ orbitals via oxygen $2p$ orbitals is extremely sensitive to the spin transfer mechanism and the angles of the Li–O–M bonds, as well as to the coordination numbers or environments of M and the intervening oxygen[12, 13, 15, 16].

The ^{23}Na MAS NMR spectrum of the ion-exchanged lithium phase, $Li_{1.1}Na_{0.4}VPO_{4.8}F_{0.7}$, shows two different isotropic peaks at 30.3 and 93 ppm (Figure S8), suggesting that two Fermi contact shifts originating from V^{4+} and V^{3+} ions still exist. In the pristine Na phase, a NMR shift of Na^+ ions around V^{4+} ions (70 ppm) and another shift of Na^+ ions around V^{3+} ions (112 ppm) in $Na_{1.5}VPO_{4.8}F_{0.7}$ were observed (see the middle spectrum in Figure 2a in the text). However, the former (related to V^{4+} ions) in the lithium phase (30.3 ppm) was far more suppressed than the latter (related to V^{3+} ions) in the lithium phase (93 ppm), implying that Na^+ ions around V^{4+} ions in the original sodium phase more actively participated in the ion-exchange process than those around V^{3+} ions. In other words, most Li^+ ions in the lithium phase probably exist around V^{4+} ions, which can explain the absence of another minor peak having a more positive isotropic shift (related to V^{3+} ions) in the ^{6}Li MAS NMR spectrum of the lithium phase (see Figure 2c in the text).

The ^{23}Na NMR shifts were different for the lithium phase and the parent sodium phase

because the NMR shifts for our paramagnetic samples were mainly governed by the Fermi contact interaction. For our $Na_{1.5}VPO_{4.8}F_{0.7}$ and $Li_{1.1}Na_{0.4}VPO_{4.8}F_{0.7}$, each Na^+ ion receives electron spins from four adjacent vanadium ions via O $2p$ (or F $2p$) orbitals, and the transferred net spin densities lead to a large sodium hyperfine shift. Various possible Na $3s$ − O $2p$ − V t_{2g} and Na $3s$ − F $2p$ − V t_{2g} interactions are schematically shown in Figure S9. In $Li_{1.1}Na_{0.4}VPO_{4.8}F_{0.7}$, hyperfine shifts originating from Na^+ ions around V^{4+} and V^{3+} ions were 30.3 and 93 ppm, respectively (Figure S8), while those in $Na_{1.5}VPO_{4.8}F_{0.7}$ were 70 and 112 ppm, respectively (the middle spectrum in Figure 2a). Less-positive shift values for the lithium phase arose from the smaller net electron spin density near a sodium nucleus being transferred from the paramagnetic V^{4+} ($t_{2g}{}^1 e_g{}^0$) and V^{3+} ($t_{2g}{}^2 e_g{}^0$) ions via O $2p$ or F $2p$ orbitals[12, 13]. Assuming that the sodium and lithium phases have a similar degree of mixing uniformity between V^{4+} and V^{3+} ions, we believe that the fewer transferred spins are attributable to a larger deviation from 90° of the Na–O(F)–V angles in the lithium phase[12, 13]. More in-depth studies on the assignment of NMR shifts are in progress.
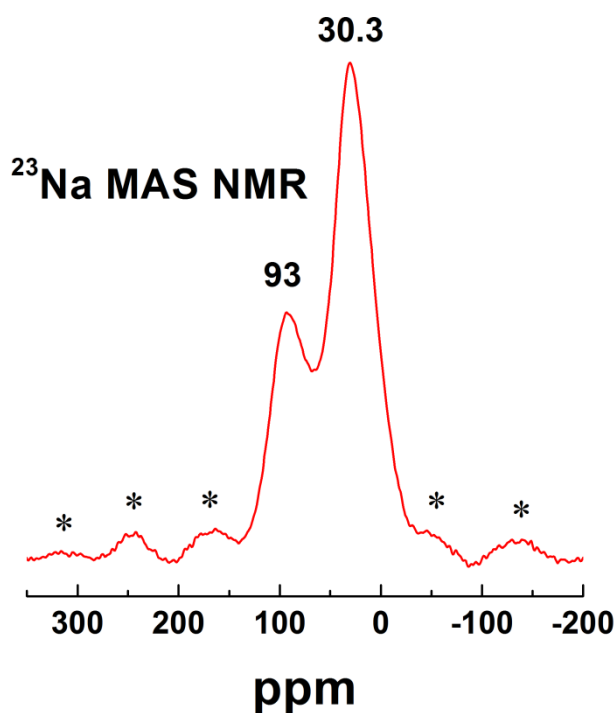
Figure S8. ^{23}Na MAS NMR spectrum of $Li_{1.1}Na_{0.4}VPO_{4.8}F_{0.7}$ at a MAS spinning speed of 15 kHz. Spinning sidebands are marked with asterisks and the NMR shifts were referenced to 0.1 M NaCl (0 ppm).
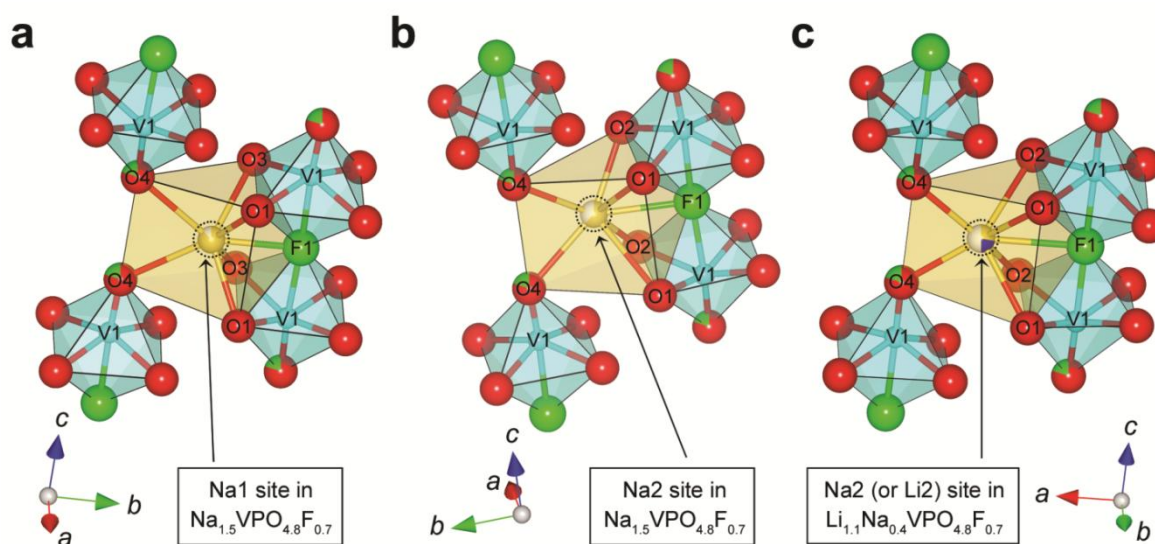

Figure S9. Several types of Na $3s$ − O $2p$ (F $2p$) − V t_{2g} interactions in (a, b) $Na_{1.5}VPO_{4.8}F_{0.7}$ and (c) $Li_{1.1}Na_{0.4}VPO_{4.8}F_{0.7}$ are schematically represented.

Chapter 8) XRD measurements of the pristine lithium phase and fully delithiated phase

We tried to obtain a fully delithiated phase of the pristine $Li_{1.1}Na_{0.4}VPO_{4.8}F_{0.7}$ to determine how much volume change occurs upon cycling. From ICP spectroscopy results and other elemental analysis, the composition of the delithiated sample was $Li_{0.01}Na_{0.41}VPO_{4.8}F_{0.7}$, hereafter, $Na_{0.4}VPO_{4.8}F_{0.7}$ for convenience. By the full pattern matching of a powder XRD pattern of the $Li_{1.1}Na_{0.4}VPO_{4.8}F_{0.7}$ (Figure S10a) and a synchrotron XRD pattern of the $Na_{0.4}VPO_{4.8}F_{0.7}$ (Figure S10b), we obtained their lattice parameters and cell volumes (Table S7). All reflections in the synchrotron XRD pattern of $Na_{0.4}VPO_{4.8}F_{0.7}$ were successfully indexed in the same space group as $Li_{1.1}Na_{0.4}VPO_{4.8}F_{0.7}$ (*P4₂/mnm*), implying that the extraction of Li^+ ions from the $Li_{1.1}Na_{0.4}VPO_{4.8}F_{0.7}$ occurs within a solid-solution range. According to Table S7, the unit cell volume difference between the fully delithiated phase ($Na_{0.4}VPO_{4.8}F_{0.7}$) and the pristine lithium phase ($Li_{1.1}Na_{0.4}VPO_{4.8}F_{0.7}$) was 0.67%.

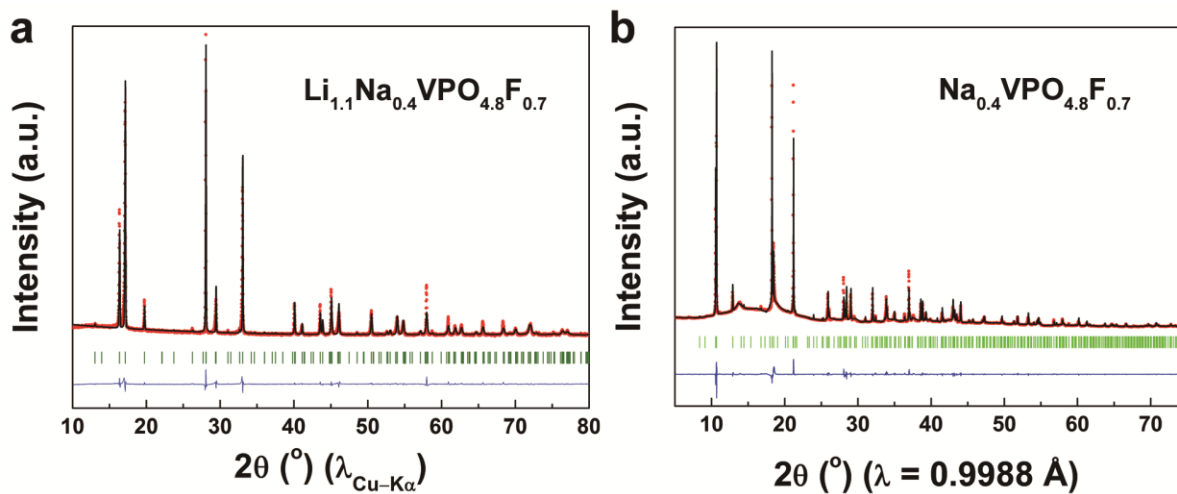**Figure S10.** (a) An X-ray powder diffraction pattern ($\lambda_{Cu-K\alpha}$) and the Rietveld refinement of $Li_{1.1}Na_{0.4}VPO_{4.8}F_{0.7}$. (b) A synchrotron XRD pattern and the Rietveld refinement of $Na_{0.4}VPO_{4.8}F_{0.7}$ with observed data points (red dots), calculated pattern (black line), difference curve (blue line), and Bragg positions (green bars).

Table S7. Lattice parameters (in the space group $P4_2/mnm$) obtained by the full pattern matching of the XRD patterns of $Li_{1.1}Na_{0.4}VPO_{4.8}F_{0.7}$ and $Na_{0.4}VPO_{4.8}F_{0.7}$

Composition	*a (Å)*	*c (Å)*	*Cell Volume (Å³)*
$Li_{1.1}Na_{0.4}VPO_{4.8}F_{0.7}$	8.9881(3)	10.4483(6)	844.08(6)
$Na_{0.4}VPO_{4.8}F_{0.7}$	8.8980(2)	10.7326(3)	849.75(3)

Chapter 9) Calculation of the lattice parameters of $Na_{1.5}VPO_5F_{0.5}$, $LiNa_{0.5}VPO_5F_{0.5}$, and $Na_{0.5}VPO_5F_{0.5}$ from first-principles

Because of various difficulties in performing the calculations for fluorine-substituted compositions (e.g., unaffordable computational costs due to oversized supercells, too many possible configurations of oxygen and fluorine ions), we examined similar but simpler systems, i.e., those having smaller supercells and containing fewer atoms in the anions with several arrangements. Specifically, simpler compositions ($Na_{1.5}VPO_5F_{0.5}$, $LiNa_{0.5}VPO_5F_{0.5}$, and $Na_{0.5}VPO_5F_{0.5}$) were used instead of $Na_{1.5}VPO_{4.8}F_{0.7}$, $Li_{1.1}Na_{0.4}VPO_{4.8}F_{0.7}$, and $Na_{0.4}VPO_{4.8}F_{0.7}$. We believe that the calculations for these slightly different compositions will still allow us to arrive at reasonable conclusions. From first-principles, we calculated various Na/Vacancy and Li/Na/Vacancy configurations to determine the ground-state structures of $Na_{1.5}VPO_5F_{0.5}$ and $LiNa_{0.5}VPO_5F_{0.5}$, respectively. The reported[17] crystal structure of $Na_{1.5}VPO_5F_{0.5}$ was used as the starting point for our calculations. Then, the ground-state structure of $Na_{0.5}VPO_5F_{0.5}$ was chosen by eliminating the more energetically unfavorable Na^+ ions in $Na_{1.5}VPO_5F_{0.5}$. Their ground-state structures are illustrated in Figure S11 with the corresponding configurations of alkali ions. All lattice parameters of $Na_{1.5}VPO_5F_{0.5}$, $LiNa_{0.5}VPO_5F_{0.5}$, and $Na_{0.5}VPO_5F_{0.5}$ were predicted via first-principles calculations using the most energetically stable structures (at 0 K). Their lattice parameters are shown for the space group $P4_2/mnm$ in Table S8. The volume change between the charged and discharged states ($\Delta V_{chg.-dchg.}$) was estimated by comparing their cell volumes. For example, the volume changes of $Na_{1.5}VPO_5F_{0.5}$ and $LiNa_{0.5}VPO_5F_{0.5}$ during charging/discharging were calculated by dividing the differences from the predicted cell volume of $Na_{0.5}VPO_5F_{0.5}$ (the structure in which one Na^+ or Li^+ ion per formula unit is extracted from each initial structure) by pristine volumes. While $Na_{1.5}VPO_5F_{0.5}$ showed a volume change of 3.1%, $LiNa_{0.5}VPO_5F_{0.5}$ exhibited

a very small volume difference (0.4%) between the charged and discharged states, which could explain its excellent cyclability.

Table S8. Lattice parameters predicted by first-principles calculations

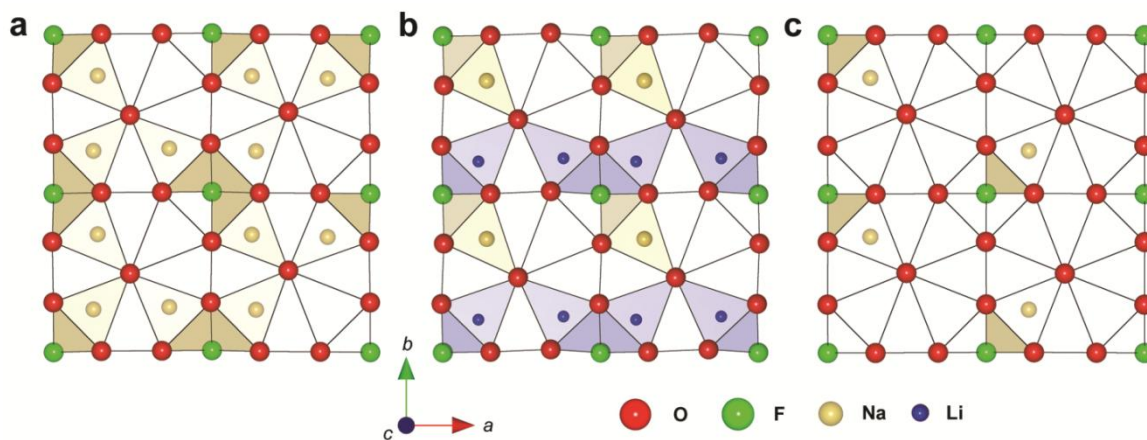| Composition	a (Å)	c (Å)	Cell Volume (Å^3)	$\Delta V_{chg.-dchg.}$
$Na_{1.5}VPO_5F_{0.5}$	9.04	10.38	848	3.1 %
$LiNa_{0.5}VPO_5F_{0.5}$	8.99	10.20	825	0.4 %
$Na_{0.5}VPO_5F_{0.5}$	8.82	10.55	822	-

Figure S11. Ground-state structures of (a) $Na_{1.5}VPO_5F_{0.5}$, (b) $LiNa_{0.5}VPO_5F_{0.5}$, and (c) $Na_{0.5}VPO_5F_{0.5}$ for the lattice parameter calculations.

Chapter 10) Structural stability of $Li_{1.1}Na_{0.4}VPO_{4.8}F_{0.7}$ upon cycling

The difference between XRD patterns of the pristine electrode and the sample in the discharged state after 100 cycles with a 1C cycling rate was insignificant (Figure S12), indicating good structural stability during charging/discharging. From EDS analysis, we found that the Na/V ratio of a pristine electrode (0.399 ± 0.017) was almost identical to that of the 100th discharged electrode (0.391 ± 0.021). This implies that Na^+ ions are immobile in the structure and do not significantly affect the structural evolution upon cycling.
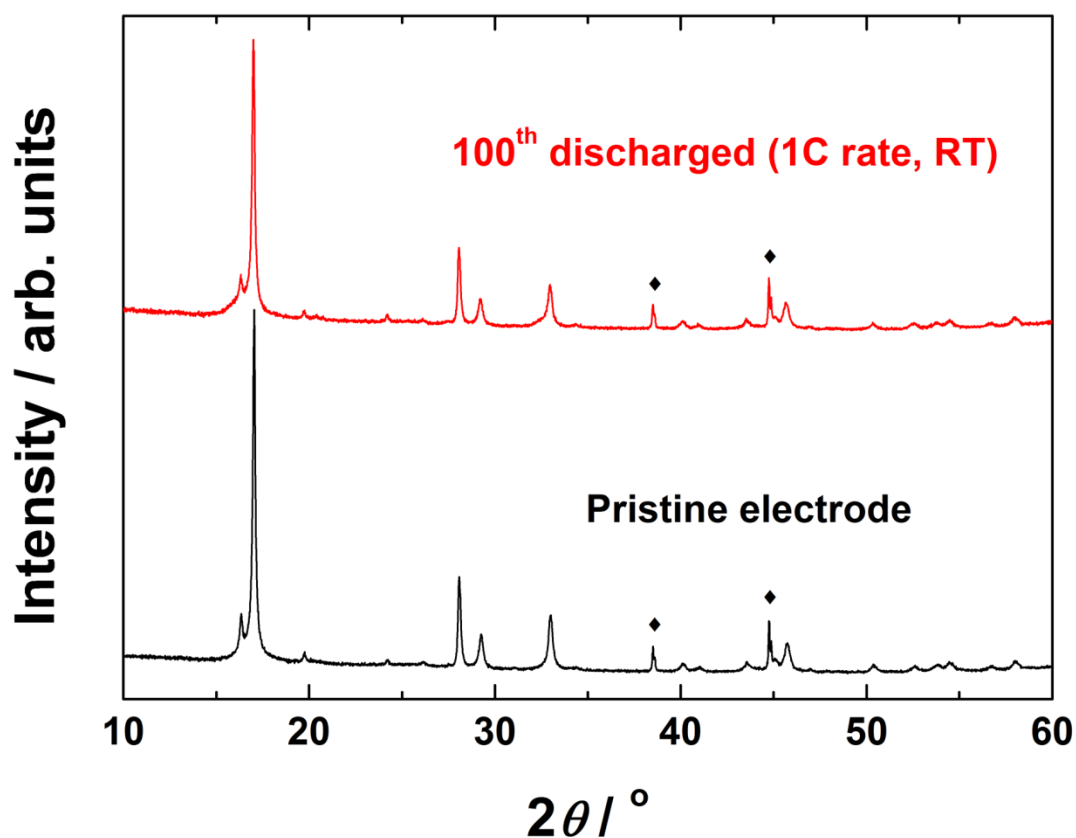

Figure S12. XRD pattern of the electrode in the discharged state after 100 cycles with a 1C cycling rate at room temperature (top red line). The bottom black line shows XRD pattern of the pristine electrode for comparison. Reflections from aluminum foil are denoted as ♦.

Chapter 11) Detailed information for the nudged-elastic-band (NEB) calculation

For the NEB calculation, we selected the initial configurations, shown in Figure S13, of the alkali ions in $Na_{1.5}VPO_5F_{0.5}$ and $LiNa_{0.5}VPO_5F_{0.5}$. These configurations have similar environments for alkali ion hopping in the initial and final states. The energies of these configurations are ca. 30 meV per formula unit higher than those of the ground-state structures (see Figure S11a and S11b). Since these small energy differences can be easily overcome with thermal energy at room temperature (ca. 25 meV), we believe that our initial configurations are suitable representations for alkali ion diffusion in $Na_{1.5}VPO_5F_{0.5}$ and $LiNa_{0.5}VPO_5F_{0.5}$.

Two diffusion pathways exist for alkali ions in $Na_{1.5}VPO_5F_{0.5}$ and $LiNa_{0.5}VPO_5F_{0.5}$, as described in the text. Path 1 follows a ring-shaped route and path 2 crosses the ring, as shown in Figure 5a. Figure S14 shows the trajectories and the corresponding activation energies for sodium and lithium hopping in diffusion path 1 in $Na_{1.5}VPO_5F_{0.5}$ and $LiNa_{0.5}VPO_5F_{0.5}$ predicted by the NEB method. Figure 5b–e (in the text) shows the trajectories and the corresponding activation energies for Na- and Li-hopping in diffusion path 2 in $Na_{1.5}VPO_5F_{0.5}$ and $LiNa_{0.5}VPO_5F_{0.5}$.
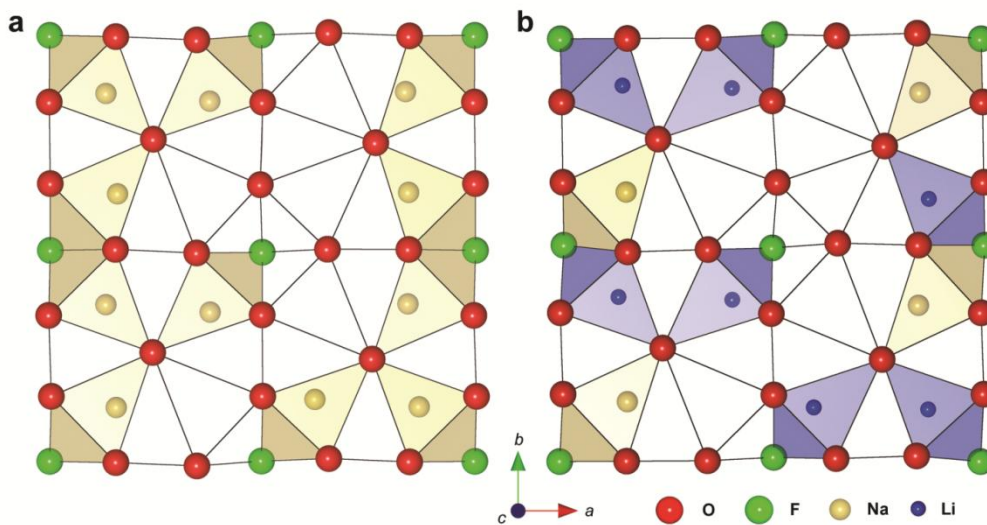
Figure S13. Initial configurations of alkali ions in (a) $Na_{1.5}VPO_5F_{0.5}$ and (b) $LiNa_{0.5}VPO_5F_{0.5}$ for the NEB calculations.

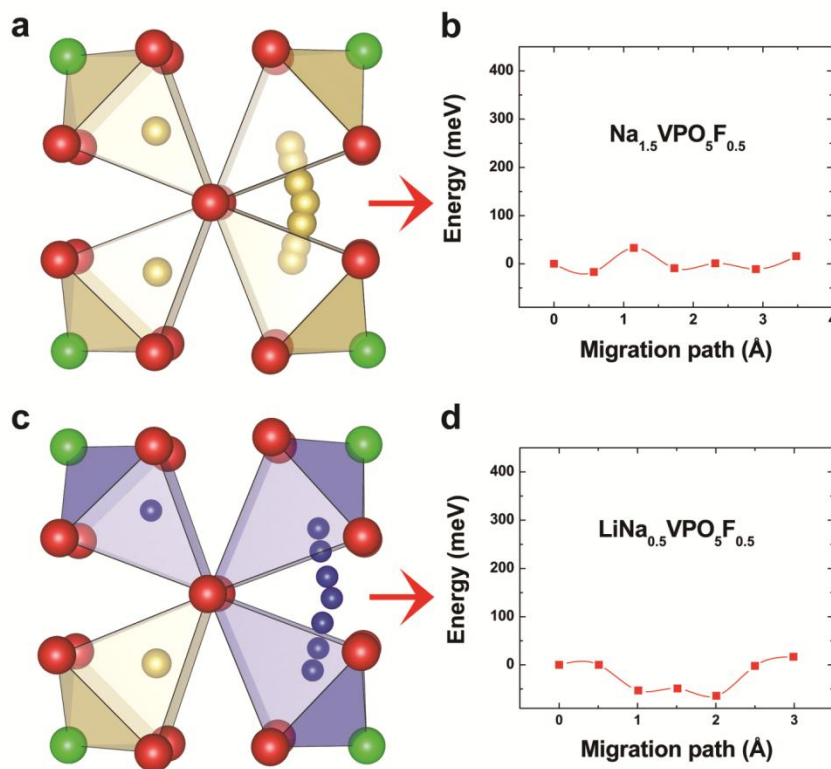**Figure S14.** (a) Trajectories and (b) corresponding activation barriers for Na hopping for diffusion path 1 in $Na_{1.5}VPO_5F_{0.5}$ as predicted by the NEB method. (c) Trajectories and (d) corresponding activation barriers for Li hopping for diffusion path 1 in $LiNa_{0.5}VPO_5F_{0.5}$ as predicted by the NEB method.

Chapter 12) Estimation of the diffusion constants of Na$_{1.5}$VPO$_5$F$_{0.5}$ and LiNa$_{0.5}$VPO$_5$F$_{0.5}$

The diffusion coefficient or diffusion constant, D, can be expressed by the following equation:

$$D = a^2 \nu^* e^{-E_a/k_B T}$$

where a is the jump distance, ν^* is the jump frequency, E_a is the activation barrier for lithium diffusion, and k_B is the Boltzmann constant[18]. Assuming that ν^* is ca. 10^{12} Hz, which is within the range of phonon frequencies, and a is approximately 5 Å, corresponding to the distance of a hop along path 2 (as defined in the text), the diffusion constants of Na$_{1.5}$VPO$_5$F$_{0.5}$ and LiNa$_{0.5}$VPO$_5$F$_{0.5}$ can be approximated as 10^{-8} and 10^{-6} cm^2 s^{-1}, respectively, at room temperature. Assuming the same pre-exponential factor of diffusivity, lithium diffusivity in LiNa$_{0.5}$VPO$_5$F$_{0.5}$ is expected to be one order of magnitude greater than the diffusion coefficients of conventional cathode materials.

Chapter 13) Carbon-coating process of the ion-exchanged Li$_{1.1}$Na$_{0.4}$VPO$_{4.8}$F$_{0.7}$

Li$_{1.1}$Na$_{0.4}$VPO$_{4.8}$F$_{0.7}$ was carbon-coated to improve its electrical conduction. After 80 wt% of the ion-exchanged Li$_{1.1}$Na$_{0.4}$VPO$_{4.8}$F$_{0.7}$ had been well blended with 20 wt% Super P through dry ball-milling, the mixture was annealed at 450℃ for 12 hours under an argon atmosphere to eliminate the residual solvent and enhance its crystallinity. The XRD patterns before and after heat treatment were the same, indicating that no phase separation or decomposition occurred (Figure S15). The carbon content (20 wt%) was also unchanged by heat treatment. A SEM image of the composite (Figure S16a) and the elemental mapping of carbon (Figure S16b) by EDS clearly show that the carbon nanoparticles were homogeneously distributed around the Li$_{1.1}$Na$_{0.4}$VPO$_{4.8}$F$_{0.7}$ microcrystallites. The EDS elemental mapping results for other elements in the same area are shown in Figure S16c–f for comparison. The carbon coating is unlikely to have deteriorated the tap density because of the large discrepancy in the particle sizes of the Li$_{1.1}$Na$_{0.4}$VPO$_{4.8}$F$_{0.7}$ powder and carbon (a few microns versus tens of nanometers). Although the carbon coating process greatly contributed to the excellent rate capability of the Li$_{1.1}$Na$_{0.4}$VPO$_{4.8}$F$_{0.7}$ electrode, the carbon coating effect was not significant at a low current rate which typically represents the intrinsic electrochemical performance of new cathode materials. Despite the absence of carbon coating process for the micron-sized Li$_{1.1}$Na$_{0.4}$VPO$_{4.8}$F$_{0.7}$ powders, electrochemical properties of the pristine (or non-coated) electrode were comparable to those of the carbon-coated electrode at the same rate of C/20, as shown in Figure S17. According to Figure S17, although the non-coated Li$_{1.1}$Na$_{0.4}$VPO$_{4.8}$F$_{0.7}$ electrode exhibited slightly higher polarization than the carbon-coated electrode during the discharge process, the first charge/discharge capacities of them were almost identical. For this reason, we believe that Figure 4b in the text represents the intrinsic material properties of Li$_{1.1}$Na$_{0.4}$VPO$_{4.8}$F$_{0.7}$ regardless of the carbon-coating.

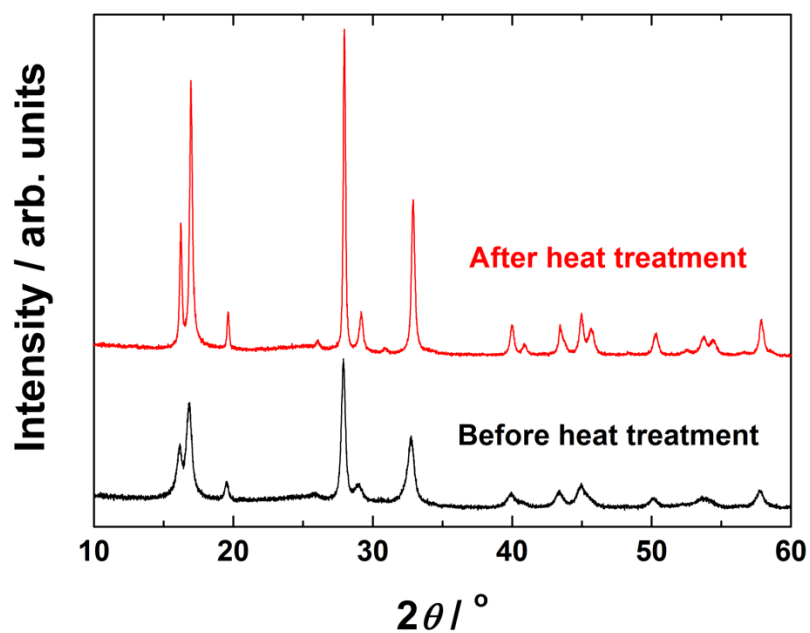**Figure S15.** XRD patterns of carbon-coated $Li_{1.1}Na_{0.4}VPO_{4.8}F_{0.7}$ before (bottom, black line) and after (top, red line) the heat treatment.

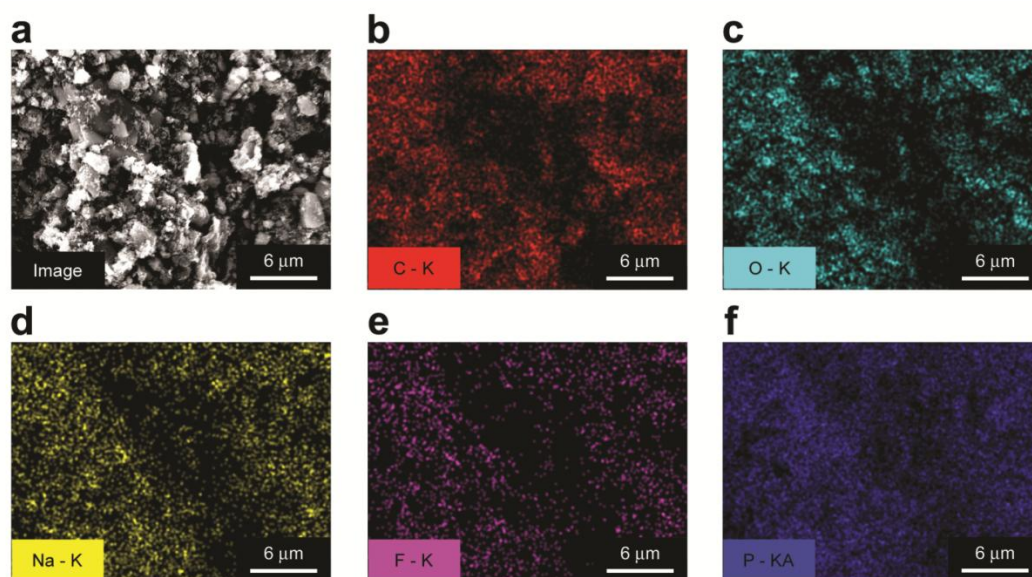**Figure S16.** (a) SEM image of carbon-coated $Li_{1.1}Na_{0.4}VPO_{4.8}F_{0.7}$ and EDS elemental mapping of (b) C, (c) O, (d) Na, (e) F, and (f) P. The material was investigated on copper tape in lieu of carbon tape to avoid confusion. The operating voltage and the working distance for the EDS measurements were 15.0 kV and 8.6 mm, respectively.
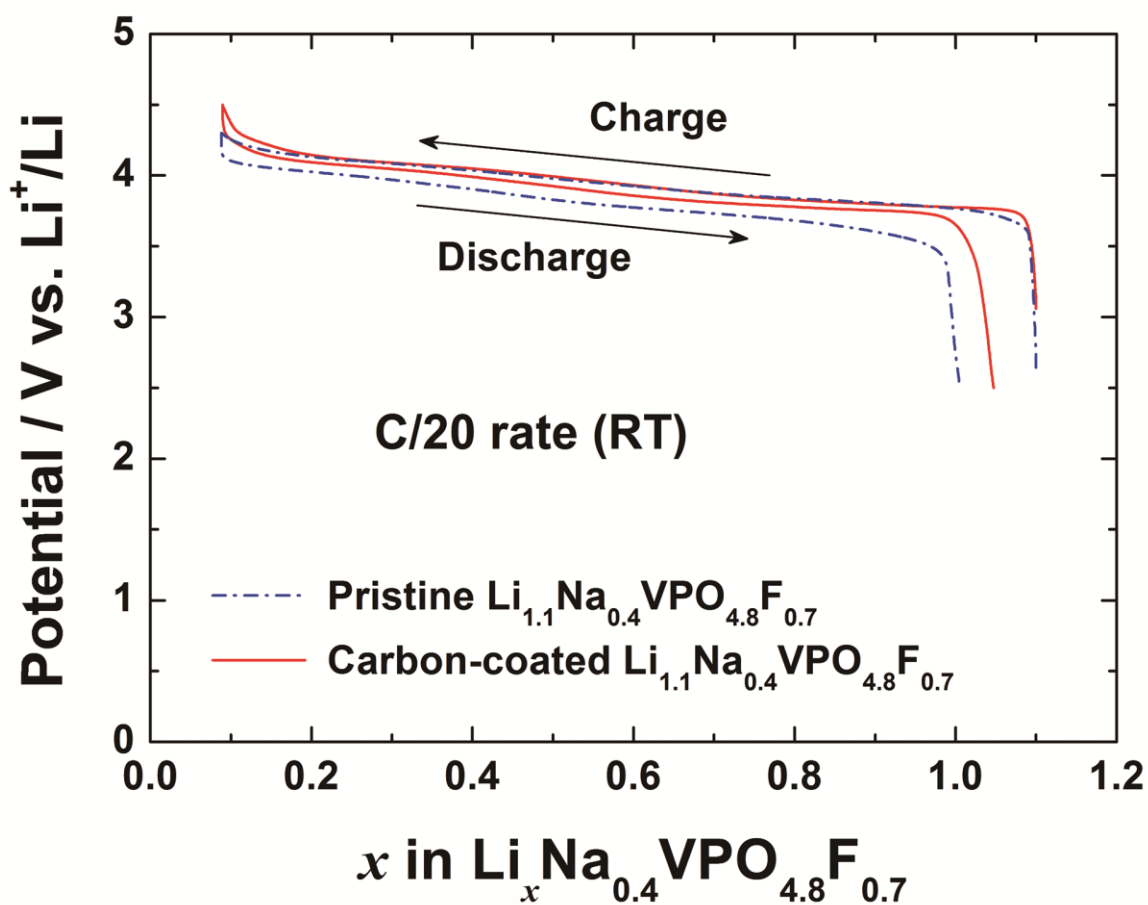
Figure S17. Galvanostatic charge/discharge curves for the first cycle of the pristine and the carbon-coated $Li_{1.1}Na_{0.4}VPO_{4.8}F_{0.7}$ electrode. The electrochemical cells were cycled at the same C/20 rate, and 1C corresponds to 156 mA g^{-1}. The voltage windows for the pristine and the carbon-coated $Li_{1.1}Na_{0.4}VPO_{4.8}F_{0.7}$ electrode were 2.5–4.3 V and 2.5–4.5 V, respectively.

References

1.   Roisnel, T. & Rodríguez-Carvajal, J. WinPLOTR: A windows tool for powder diffraction pattern analysis. *Mater. Sci. Forum* **378-381**, 118-123 (2001).

2.   Cullity, B. D. & Stock, S. R. *Elements of X-ray Diffraction*. Vol. 3 (Prentice hall Upper Saddle River, NJ, 2001).

3.   Bocquet, A. E., Mizokawa, T., Saitoh, T., Namatame, H. & Fujimori, A. Electronic structure of 3d-transition-metal compounds by analysis of the 2p core-level photoemission spectra. *Phys. Rev. B* **46**, 3771-3784 (1992).

4.   Nag, N. K. & Massoth, F. E. Esca and gravimetric reduction studies on V/Al_2O_3 and V/SiO_2 catalysts. *J. Catal.* **124**, 127-132 (1990).

5.   Silversmit, G., Depla, D., Poelman, H., Marin, G. B. & De Gryse, R. Determination of the V2p XPS binding energies for different vanadium oxidation states (V5+ to V0+). *J. Electron. Spectrosc. Relat. Phenom.* **135**, 167-175 (2004).

6.   Šalkus, T. *et al.* Preparation and characterization of $Li_{2.9}Sc_{1.9-y}Y_yZr_{0.1}(PO_4)_3$ (where y = 0, 0.1) solid electrolyte ceramics. *Phase Transitions* **83**, 581-594 (2010).

7.   Hodnett, B. K., Permanne, P. & Delmon, B. Influence of p/v ratio on the phase composition and catalytic activity of vanadium phosphate based catalysts. *Applied Catalysis* **6**, 231-244 (1983).

8.   Yin, S. C., Strobel, P. S., Grondey, H. & Nazar, L. F. $Li_{2.5}V_2(PO_4)_3$: A room-temperature analogue to the fast-ion conducting high-temperature γ-phase of $Li_3V_2(PO_4)_3$. *Chem. Mater.* **16**, 1456-1465 (2004).

9.   Cushing, B. L. & Goodenough, J. B. $Li_2NaV_2(PO_4)_3$: A 3.7 V Lithium-insertion cathode with the rhombohedral NASICON structure. *J. Solid State Chem.* **162**, 176-

181 (2001).

10.   Clearfield, A. Role of ion-exchange in solid-state chemistry. *Chem. Rev.* **88**, 125-148 (1988).

11.   Li, Z., Zhang, D. & Yang, F. Developments of lithium-ion batteries and challenges of $LiFePO_4$ as one promising cathode material. *J. Mater. Sci.* **44**, 2435-2443 (2009).

12.   Grey, C. P. & Dupre, N. NMR studies of cathode materials for lithium-ion rechargeable batteries. *Chem. Rev.* **104**, 4493-4512 (2004).

13.   Carlier, D., Ménétrier, M., Grey, C. P., Delmas, C. & Ceder, G. Understanding the NMR shifts in paramagnetic transition metal oxides using density functional theory calculations. *Phys. Rev. B* **67**, 174103 (2003).

14.   Goodenough, J. B. *Magnetism and the Chemical Bonds*. (Wiley, New-York, 1963).

15.   Lee, Y. J. & Grey, C. P. ^{6}Li magic-angle spinning (MAS) NMR study of electron correlations, magnetic ordering, and stability of lithium manganese(III) oxides. *Chem. Mater.* **12**, 3871-3878 (2000).

16.   Pan, C., Lee, Y. J., Ammundsen, B. & Grey, C. P. ^{6}Li MAS NMR studies of the local structure and electrochemical properties of Cr-doped lithium manganese and lithium cobalt oxide cathode materials for lithium-ion batteries. *Chem. Mater.* **14**, 2289-2299 (2002).

17.   Sauvage, F., Quarez, E., Tarascon, J. M. & Baudrin, E. Crystal structure and electrochemical properties vs. Na^+ of the sodium fluorophosphate $Na_{1.5}VOPO_4F_{0.5}$. *Solid State Sci.* **8**, 1215-1221 (2006).

18.   Shewmon, P. *Diffusion in solids*. (Minerals, Metals & Materials Society, 1989).